

Article

Aluminium-Silicon Lightweight Thermal Management Alloys with Controlled Thermal Expansion

Peter Lewis ^{1,*} , Andrew Tarrant ¹, Andreas Frehn ², Fritz Gensing ³, James Nicholson ¹, Nick Farrah ³ and Martyn Acreman ³

¹ Materion UK Ltd., Farnborough GU14 6XE, UK

² Materion Brush GmbH, 70499 Stuttgart, Germany

³ Materion Corporation, Mayfield Heights, OH 44124, USA

* Correspondence: peter.lewis@materion.com

Abstract: With the ever-growing emphasis on global decarbonization and rapid increases in the power densities of electronics equipment in recent years, new methods and lightweight materials have been developed to manage heat load as well as interfacial stresses associated with coefficient of thermal expansion (CTE) mismatches between components. The Al–Si system provides an attractive combination of CTE performance and high thermal conductivity whilst being a very lightweight option. Such materials are of interest to industries where thermal management is a key design criterion, such as the aerospace, automotive, consumer electronics, defense, EV, and space sectors. This paper will describe the development and manufacture of a family of high-performance hypereutectic Al–Si alloys (AyontEX™) by a powder metallurgy method. These alloys are of particular interest for structural heat sink applications that require high reliability under thermal cycling (CTE of 17 $\mu\text{m}/(\text{m}\cdot^\circ\text{C})$), as well as reflective optics and instrument assemblies that require good thermal and mechanical stability (CTE of 13 $\mu\text{m}/(\text{m}\cdot^\circ\text{C})$). Critical performance relationships are presented, coupled with the microstructural, physical, and mechanical properties of these Al–Si alloys.

Keywords: CTE; heatsink; HIP; hypereutectic; mechanical alloying; metal matrix composite; MMC; powder metallurgy; reflective optics; thermal stability



Citation: Lewis, P.; Tarrant, A.; Frehn, A.; Gensing, F.; Nicholson, J.; Farrah, N.; Acreman, M. Aluminium-Silicon Lightweight Thermal Management Alloys with Controlled Thermal Expansion. *Crystals* **2024**, *14*, 455. <https://doi.org/10.3390/cryst14050455>

Academic Editor: Shouxun Ji

Received: 28 March 2024

Revised: 30 April 2024

Accepted: 3 May 2024

Published: 11 May 2024



Copyright: © 2024 by the authors. Licensee MDPI, Basel, Switzerland. This article is an open access article distributed under the terms and conditions of the Creative Commons Attribution (CC BY) license (<https://creativecommons.org/licenses/by/4.0/>).

1. Introduction

With the ever-growing emphasis on global decarbonization and rapid increases in the power densities of electronics equipment in recent years, thermal management has become an escalating engineering challenge. Thus, emphasis on designing systems that allow heat to be transported, stored, or expelled in a manner that enables key system elements to operate with high reliability within a specific temperature range is essential [1]. This raises a need for new methods and lightweight materials to manage heat load as well as interfacial stresses associated with coefficient of thermal expansion (CTE) mismatches between components. Example materials include metal matrix composites (MMCs), such as aluminium–silicon carbide (Al–SiC) and beryllium–beryllium oxide (Be–BeO). However, metallic systems, such as aluminum–beryllium (Al–Be) and aluminum–silicon (Al–Si) alloys, can also be applicable. Each of these material systems presents a unique set of performance properties and manufacturing challenges.

The Al–Si system provides an attractive combination of tailorable CTE and high thermal conductivity, while supporting a lightweight design. Al–Si alloys are of interest for structural heat sink applications that require high reliability under thermal cycling, where a CTE of 17 $\mu\text{m}/(\text{m}\cdot^\circ\text{C})$ is desirable to minimize strain due to CTE mismatch between mating copper components. Reflective optics and instrument assemblies are also application areas, in which a CTE close to 13 $\mu\text{m}/(\text{m}\cdot^\circ\text{C})$ is necessary to match the nickel plating typically applied to such components whilst providing good thermal stability over broad operating temperature ranges [2–5].

The production of high Si Al-based alloys via traditional liquid-state processing routes can be problematic due to the challenges posed in achieving good control of the size and morphology of the primary Si phase [6]. Often this can mean that complex alloying additions or unique solidification processing methods are necessary to achieve the properties required for high-performance applications [7,8]. In contrast, manufacturing via a powder metallurgy route enables a wider range of compositions and can provide greater strength and homogeneous-microstructure-associated mechanical integrity [9,10]. Furthermore, powder metallurgy can provide near-net shape capability, which has been proven to lead to reduced waste generation and lower energy consumption per unit mass in comparison to traditional forming methods [11]. By processing in the solid-state, any possible detrimental diffusional or chemical reactions between constituent phases can be minimized. Avoiding molten processing allows the creation of non-equilibrium phase structures. This enables extensive opportunities for novel and interesting material combinations to enhance performance beyond traditional engineering materials.

Mechanical alloying is a solid-state mixing process in which MMC materials and metallic alloys are combined using powder metallurgy methods. As no melting is required, the reinforcement volume fraction and particle size are controlled by raw material selection. Thereby, this process enables precise control of reinforcement particle sizes with higher reinforcement volume fractions, both of which are critical in maximizing and optimizing the property benefits that can be achieved with MMC systems relative to the monolithic material [12]. Mechanical alloying was first developed in the 1960s with the aim of fabricating a nickel-based superalloy with homogeneous distribution of oxide reinforcements for gas turbine applications [13]. Since then, many material combinations have been explored [14–26]. The basic principle is the cyclical welding and fracture of ductile and brittle powders via repetitive impact, resulting in a distribution of reinforcement within the metallic matrix particles [27]. However, the optimization of key parameters is necessary to achieve a homogeneous and stable process [24–26,28,29]. This composite powder then acts as an input into downstream consolidation processes, such as hot isostatic pressing (HIP) or extrusion.

Materion’s mechanical alloying and powder metallurgy technologies have been used for decades to produce commercially available particle reinforced aluminium–SiC SupremEX[®] MMCs [30–32]. It should be noted that the industrial scale of this technology is highly unique. The total capacity of Materion UK’s mechanical alloying facility is 300 MT per annum. It is understood that light alloy mechanical alloying capability at this scale does not exist anywhere else in the world. A schematic summarizing this powder metallurgy route is given by Figure 1. These MMCs have been shown to display a very fine and homogeneous microstructure, with precise control of particle sizes [33]. The resultant composite materials are known to be isotropic with high modulus, strength, wear, and fatigue performance [30,34], but maintain the machining, fabrication, coating, and processing characteristics of conventional aluminium alloys.

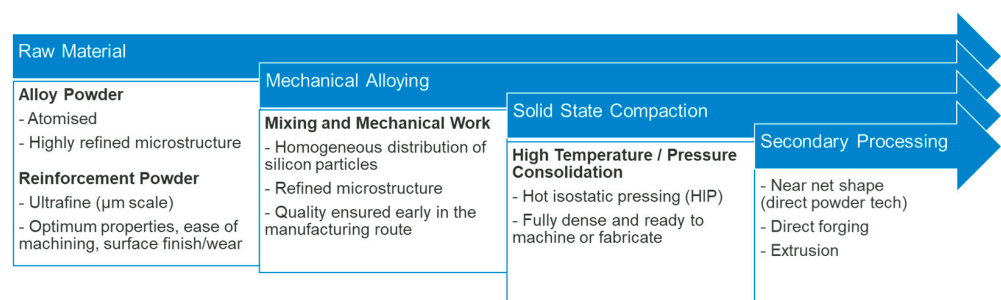


Figure 1. Schematic summarizing Materion’s mechanical alloying powder metallurgy routes.

This paper will describe manufacturing of hypereutectic Al–Si alloys via a powder metallurgy route utilizing Materion’s novel mechanical alloying process. Due to the flexibility of the manufacturing route, this lightweight material system has been finely

tuned to achieve the specific and desirable CTE values referenced above. A detailed understanding of the relationship between chemistry and CTE has been developed. Critical performance relationships such as this will be presented, coupled with the microstructure and physical and mechanical properties of these Al–Si alloys.

2. Materials and Methods

The powder metallurgy processing described by Figure 1 and [30,31] was leveraged to combine elemental Si with Al alloy powders. The powder mixtures were mechanically alloyed until the Si was distributed within the Al matrix, with an overall refined and homogeneous microstructure. To achieve an optimal balance of mechanical and thermal properties, a 6063-alloy composition was selected, along with high-purity silicon powders. A series of samples with chemistry ranging from 15–55 wt% Si were processed. Initially the mechanically alloyed powder was loaded in a vibratory manner into an aluminium can, before degassing at an elevated temperature under vacuum conditions to eliminate air and any absorbed water vapor. Following this, the HIP process was applied to form fully dense cylindrical billets of material, approximately $\text{Ø}100 \text{ mm} \times 170 \text{ mm}$ in size. This compaction method is summarized by Figure 2.

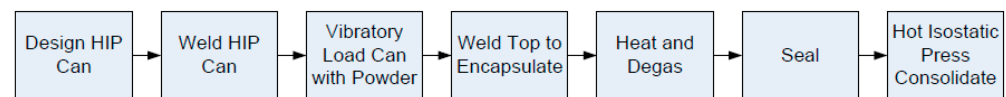


Figure 2. Major steps to HIP consolidate Al–Si powders made by the mechanical alloying process.

Samples for CTE evaluation were extracted from these billets and tested per ASTM E228-17 in order to understand the relationship between composition and this critical property. The samples were heat treated to a T6 condition prior to CTE measurement using the following method: solution treatment at 535 °C for 1 h, followed by a cold water (<30 °C) quench (CWQ), and finally, artificial aging at 175 °C for 2 h. All test samples were heat treated with a maximum section thickness less than or equal to 25 mm.

This initial CTE evaluation enabled derivation of the necessary compositions to achieve a CTE close to the target values of 17 $\mu\text{m}/(\text{m}\cdot^\circ\text{C})$ and 13 $\mu\text{m}/(\text{m}\cdot^\circ\text{C})$ at 28% and 42% Si, respectively. This is depicted graphically by Figure 3. Larger scale cylindrical billets (approx. $\text{Ø}150 \text{ mm} \times 600 \text{ mm}$) and cuboid billets (approx. $180 \text{ mm} \times 180 \text{ mm} \times 300 \text{ mm}$) were subsequently manufactured at the derived compositions using the same manufacturing conditions to confirm the scalability of the process. These materials were then tested in detail to confirm their microstructure, room temperature tensile properties, density, and electrical conductivity. Tensile testing was carried out using an Instron 3369 loading frame with a 50 kN capacity. Multiple heat treatments were assessed, including the T6 CWQ heat treatment condition defined above, but also the same heat treatment using a 25% polymer-glycol quench (PGQ) medium, as well as the T1 (air-cooled from HIP) condition. Cylindrical specimens were used, with a 5 mm diameter and 25 mm gauge length. Test control was by a constant strain rate of $1.4 \times 10^{-4} \text{ mm}/\text{mm}/\text{s}$, until failure. Microstructural analysis was completed using a Zeiss AxioLab5 optical microscope equipped with ZEN core imaging software. CTE was again evaluated per ASTM E228-17 but over a broader temperature range of $-100 \text{ }^\circ\text{C}$ to $200 \text{ }^\circ\text{C}$, whilst room temperature thermal diffusivity and specific heat capacity were measured per ASTM E1461-13 and ASTM E1269-11, respectively. This thermal testing was carried out for both the T6 PGQ and T1 heat treatment conditions described above, to assess sensitivity of these properties to heat treatment. Thermal conductivity was calculated as the product of thermal diffusivity, specific heat capacity, and density, per Equation (1) of ASTM E1461-13 [35]. Finally, a series of components representing example applications for each of the alloy components were produced, to assess manufacturability.

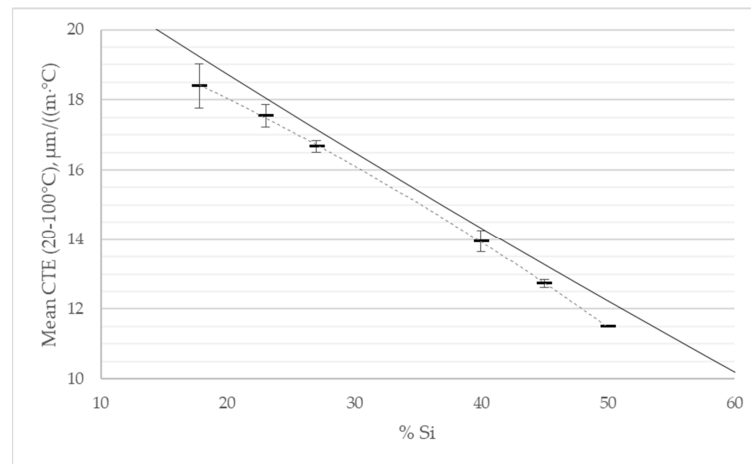


Figure 3. Effect of Si content on the CTE of the manufactured Al–Si alloys (dashed line) versus the simple rule of mixtures calculation (solid line). Data points are presented as mean values with 90% confidence intervals, where multiple tests were completed.

3. Results

3.1. Microstructure

An ultra-fine and homogeneous distribution of Si particles within the Al alloy was achieved for all Si contents tested, as Figure 4 shows. It can also be observed that the mechanically alloyed powder was generally blocky and irregular in shape across all compositions. This was consistent with past Al–SiC materials mechanically alloyed by the same process [30,31]. In the consolidated (post-HIP) form, the microstructure was seen to be consistent in all tested directions, indicating isotropic properties as expected. Typical optical micrographs of the 6063 + 42% Si alloy are presented Figure 5. Here, the ultrafine and homogeneous microstructure is again evident. The primary silicon size was observed to be an average of 3–4 μm in diameter, with almost all silicon particles within the 1–7 μm range.

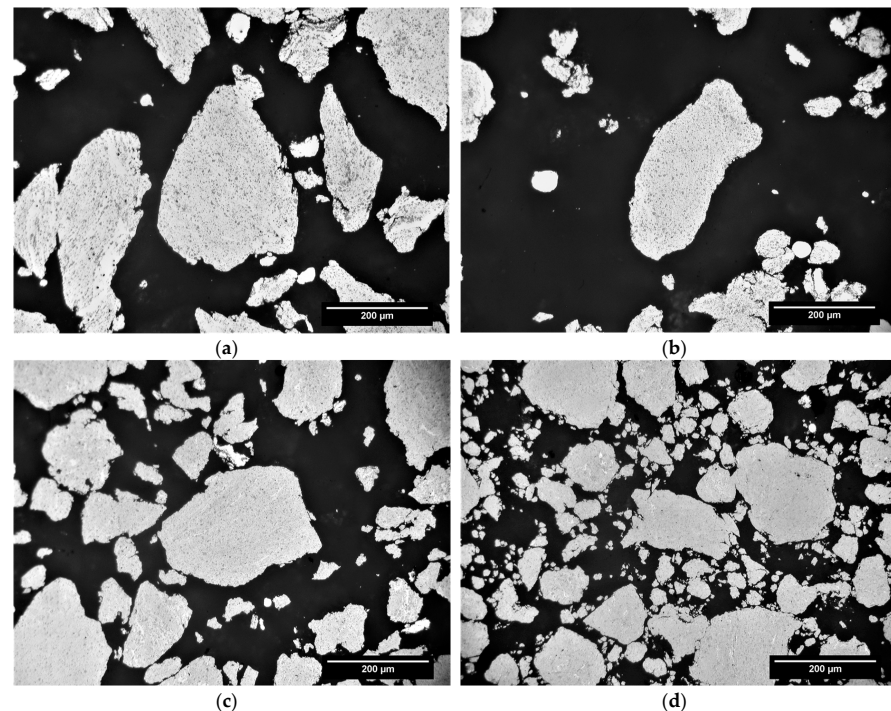


Figure 4. Mechanically alloyed Al–Si powders at (a) 18 wt% Si, (b) 27 wt% Si, (c) 40 wt% Si, and (d) 55 wt% Si (scale is intentionally withheld).

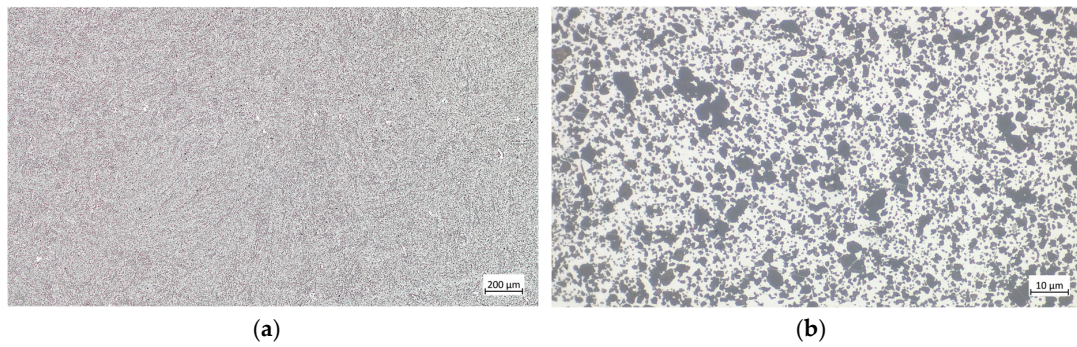


Figure 5. AyontEX 13 HIP-processed billet optical micrographs at (a) 50× magnification and (b) 1000× magnification.

3.2. Coefficient of Thermal Expansion

The achieved CTE matches to commercially pure copper and nickel are summarized by Figure 6 via comparison to reference data from the literature [36–39]. This shows an exact mean CTE match to copper for the 20–50 °C temperature range. The 28% Si alloy was determined to have a marginally lower CTE for temperatures below room temperature and a marginally higher CTE at temperatures greater than 50 °C. The mean CTE value at all temperatures, as well as the rate of change of CTE with respect to temperature for the Al–Si alloy, was significantly lower than that of unreinforced aluminium alloys (~23 $\mu\text{m}/(\text{m}\cdot^\circ\text{C})$), thus providing a relatively excellent CTE match to copper. The prior heat-treatment condition of this Al–Si alloy was seen to have negligible influence over the temperature range tested.

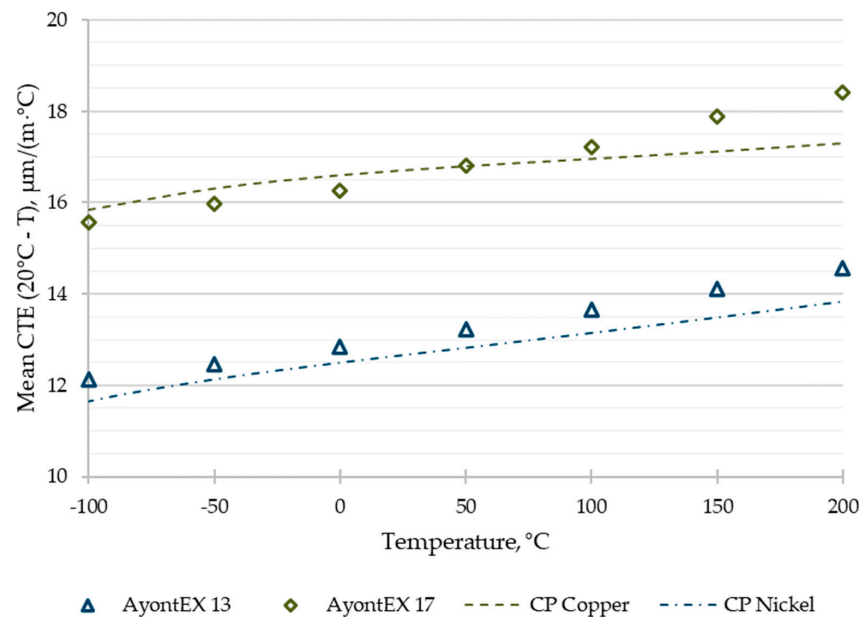


Figure 6. Achieved CTE matches to reference data on commercially pure copper and nickel.

A close CTE match was observed to nickel, with the 42% Al–Si alloy displaying a marginally higher CTE for the temperatures tested. The rate of change of CTE with respect to temperature for this Al–Si alloy and nickel was similar over the temperature range tested. Again, no influence of the prior heat treatment condition was observed.

3.3. Additional Physical and Mechanical Properties

Beyond CTE, the additional key material properties of the tested Al–Si alloys are presented in Table 1. A good balance of strength and conductivity for thermal management

applications was displayed by these alloys. Given the large ranges in strength for AyontEX 17 quoted in Table 1, typical engineering stress–strain curves for this alloy are provided in Figure 7 and true stress–strain equivalents can be seen in Figure 8.

Table 1. Summary of achieved typical properties. Ranges indicate dependence on heat treatment.

Property	Unit	AyontEX 17	AyontEX 13
Composition	-	6063 + 28% Si	6063 + 42% Si
Density	g/cm ³	2.60	2.54
Elastic Modulus	GPa	87	103
Specific Stiffness	Gpa/g/cm ³	33	41
Mean CTE	(−100–20 °C)	15.6	12.1
	(20–50 °C)	16.8	13.2
	(20–100 °C)	17.2	13.7
	(20–200 °C)	18.4	14.6
Thermal Conductivity	W/mK	160–170	134
Specific Heat Capacity	J/g/K	0.88	0.85
0.2% Proof Strength	Mpa	170–300	300–340
Ultimate Tensile Strength	Mpa	240–355	325–345
Specific Strength	Mpa/g/cm ³	92–137	128–136

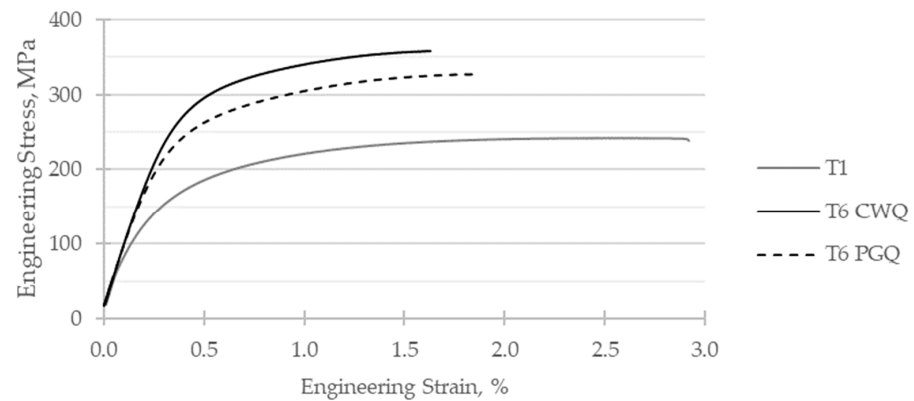


Figure 7. Typical room temperature engineering tensile stress–strain curves for AyontEX 17 alloy in different heat treatment conditions. T1 = air cooled from HIP, CWQ = cold water quench, PGQ = 25% polyglycol solution quench.

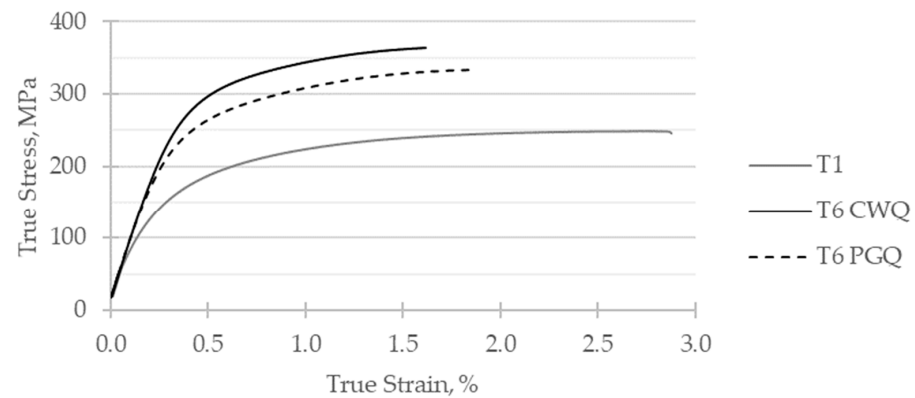


Figure 8. Typical room temperature tensile true stress–strain curves for AyontEX 17 alloy in different heat treatment conditions. T1 = air cooled from HIP, CWQ = cold water quench, PGQ = 25% polyglycol solution quench.

4. Discussion

The simple rule of mixtures calculation model provided a close approximation to the measured relationship between CTE and Si content, as shown by Figure 3. The measured values were consistently slightly lower than predicted and trended away from the model at lower and higher Si content values. A possible explanation for this deviation between the model and the measured values is that the rule of mixtures calculation does not account for phases other than the constituent elements (e.g., Mg_2Si precipitates), or the different elastic properties of the matrix, reinforcement, and associated thermal strains [40]. Particularly at the more extreme values of Si reinforcement ($\geq 50\%$), the so-called percolation threshold may have been passed, meaning it would be inappropriate to consider the Si phase and the elastic region surrounding it to be individual particles, but more likely a continuous path of reinforcement [41]. This could explain the increased deviation from the model observed at the highest Si contents tested. The negligible effect of heat treatment condition on the CTE of these alloys can be explained by the high Si content necessary to achieve such low CTEs. This thereby limits the ability to influence properties via heat treatment.

The compositions of the two now-commercially-available alloys, AyontEX 17 (with a CTE of $17 \mu\text{m}/(\text{m}\cdot^\circ\text{C})$) at 28% Si and AyontEX 13 (with a CTE of $13 \mu\text{m}/(\text{m}\cdot^\circ\text{C})$) at 42% Si, were derived from the measured CTE curve in Figure 3 as described in Section 3. The fine and homogeneous microstructures achieved (Figures 4 and 5) are important in enabling the application of high-throughput and available downstream machining and finishing processes to these alloys. Ease of machinability relative to equivalent liquid-state processed Al–Si alloys or other lightweight, low-CTE materials (e.g., MMCs) can provide a significant benefit in overall part cost by increasing throughput and decreasing tooling costs. Such benefits can be clearly realized in the manufacture of complex, high-performance components, where fine surface finish and high tolerance is required. Several common machining processes, including milling, turning, drilling, tapping, and electrical discharge machining (EDM), have been successfully performed on this material, many of which are highlighted by Figure 9. Here, the thin wall sections at the top of the part are 0.8 mm thick, and the EDM-processed slot at bottom is 0.5 mm thick and 32 mm deep. These features were achieved with standard, high-throughput methods using no special parameters.



Figure 9. Demonstration of machining process on AyontEX 17 material, highlighting ability to machine thin-wall structures and tap holes (top-right) and EDM-processed 0.5 mm slot (left).

Example components representing typical applications for each of the alloys are presented by Figure 10. The miniature structural heatsink in Figure 10a is $58 \text{ mm} \times 40 \text{ mm} \times 5 \text{ mm}$ in size, highlighting the ability to carry out precise milling, drilling, and tapping operations with the AyontEX 17 material. The AyontEX 13 mirror substrate presented by Figure 10b was approx. 150 mm in diameter. This was produced via rough machining using standard carbide tooling and completed with poly-crystalline diamond tooling. Given the low-density ($2.54 \text{ g}/\text{cm}^3$) and complex lightweighting geometry, this mirror had a mass of 0.2 kg. Such lightweight mirror design is highly beneficial for airborne applications. More detailed demonstration of lightweight mirror manufacture in this material and associated application-specific testing has been covered elsewhere [42,43].

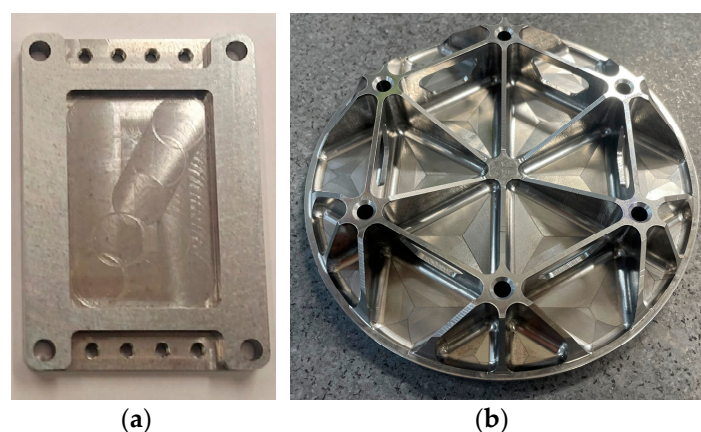


Figure 10. Example applications of the Al–Si alloys. (a) Structural heat sink manufactured in AyontEX 17. (b) Optical mirror substrate manufactured in AyontEX 13.

An emerging topic in lightweight optical mirror design is additive manufacturing to enable complex structures for material and load optimization [44–46]. It is then an interesting topic for future exploration to develop and apply additive manufacturing techniques to the AyontEX 13 material, given this alloy already exists in a powder form, as per the powder metallurgy route presented here. Such development would combine the material property benefits discussed here with the design freedom of additive manufacturing for high-performance applications.

Close CTE matches with mating materials are important in the applications discussed above. The results presented in Figure 6 confirm that precise CTE matches to the reference data for copper and nickel materials were achieved with the manufactured alloys over the full -100 – 200 °C test range. Particularly, for AyontEX 13, the rate of change of CTE with respect to temperature was very consistent with that of commercially pure nickel. This is important for reflective optical and instrument systems, where precise CTE matches to nickel plating layers are critical for both dimensional and thermal stability over broad operating conditions [2–5,42,43]. It should be noted that in the case of electroless plating, the nickel material will contain some level of phosphorus. The CTE curve for NiP [3,4,47], is very similar to the commercially pure nickel CTE data used for comparison in Figure 6. It can therefore be said the AyontEX 13 material provides an excellent CTE match to both electrolytic and electroless Ni plating for application in high-precision optical mirrors. Of course, the ability to Ni plate the material is critical for such applications. An example of successful application of electrolytic nickel plating to AyontEX 13 is given by Figure 11. Electroless NiP plating solutions are also compatible [43], should this be preferred for the application.

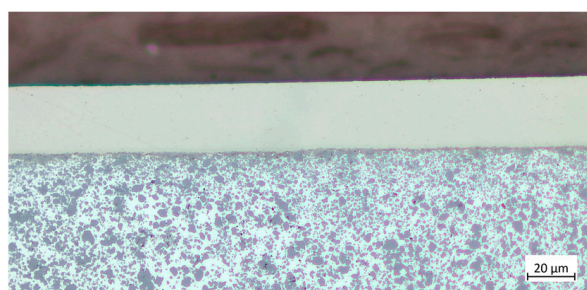


Figure 11. Optical micrograph of AyontEX 13 with electrolytic nickel plating applied, at 500× magnification.

The prior heat treatment condition of the material (T1 v. T6) was seen to have negligible impact on CTE for all compositions tested. It can therefore be understood that controlling

the thermal expansion of these hypereutectic Al–Si alloys is best achieved through adjusting the Si content, as opposed to via heat treatment optimization.

As expected, increasing the Si content resulted in a linear decrease in density and a linear increase in elastic modulus. Increasing Si content was seen to result in a decrease in thermal conductivity, but also a decrease in the dependence of heat treatment condition on the thermal conductivity. For AyontEX 17 (6063 + 28% Si), the mean thermal conductivity was determined to be 160 W/mK in the T6 condition, but 170 W/mK in the T1 (air-cooled from HIP) condition, a difference of ~6%. In contrast, for AyontEX 13 (6063 + 42% Si), the heat treatment condition was found to have a negligible impact on the thermal conductivity.

This high thermal conductivity of AyontEX 17 in the T1 condition, coupled with the precise CTE match to Cu over the 0–100 °C temperature range (see Figure 6), highlights the materials' applicability for use in lightweight structural heatsink assemblies. As a direct replacement for 6061 Al, for example, AyontEX 17 provides an increased modulus and decreased CTE and density, whilst maintaining thermal conductivity. This is critical in enabling high power density devices, where heat load must be efficiently managed, as well as interfacial stresses driven by CTE mismatches to mating Cu components.

Similar trends with respect to Si loading were observed regarding the mechanical properties, and in particular the yield strength. The 0.2% proof strength of AyontEX 17 was seen to almost double from 170 MPa in T1 to 300 MPa in T6, with significant differences in ultimate tensile strength and strain to failure. These differences are depicted by the stress–strain curves given by Figures 7 and 8. This data was generated on billet material directly following the HIP process. The application of secondary forming processes, such as forging and extrusion, will enhance the ductility of the finished product. This remains an interesting topic for further exploration to allow close to shape forming operations. By comparison, the mechanical properties in the higher Si vol% materials had a much lower dependence on the heat treatment condition, as outlined by Figures 12 and 13. These effects can be explained by simply considering that as the Si vol% was increased, the vol% of the 6063-alloy decreased. This in turn meant that less Mg was available within the alloy for Mg₂Si precipitation strengthening effects through heat treatment. Additionally, as the quantity of the primary Si phase particles was increased, the relative distance between adjacent Si particles was decreased, and thus strengthening because of the primary Si phase became a more dominant mechanism relative to the Mg₂Si precipitation phases.

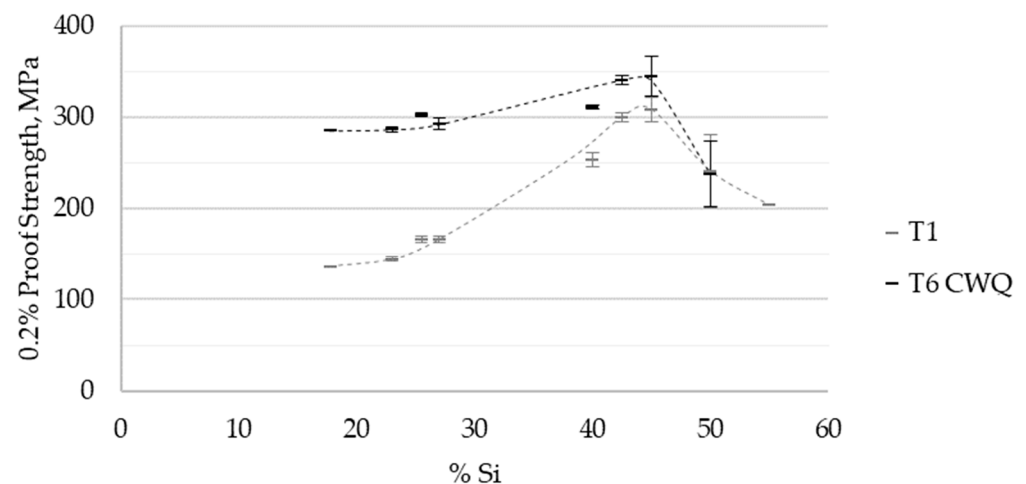


Figure 12. Relationship between 0.2% proof strength versus Si vol% and heat treatment condition. Data points are presented as mean values with 90% confidence intervals, where multiple tests were completed. T1 = air cooled from HIP, CWQ = cold water quench.

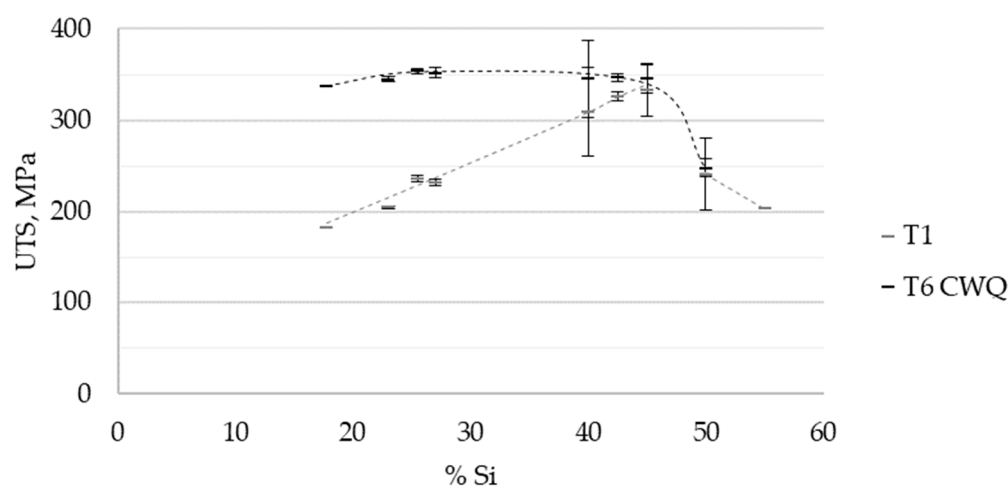


Figure 13. Relationship between ultimate tensile strength versus Si vol% and heat treatment condition. Data points are presented as mean values with 90% confidence intervals, where multiple tests were completed. (T1 = air cooled from HIP, CWQ = cold water quench).

The increasing influence of the Si phase as the Si vol% was increased to more extreme values ($\geq 50\%$) led the ensuing material to become more brittle. This resulted in an associated decrease in both 0.2% proof strength and ultimate tensile strength, as captured by Figures 12 and 13. For such compositions, the proportion of the primary Si phase is so significant that fracture can occur at the alloy–Si particle interface, due to Si particle clustering or the percolation effects described above. The severity of such effects within particulate MMC materials is well understood [48]. In contrast, at a more modest Si vol%, such as those used for the AyontEX 17 and AyontEX 13 materials, fracture occurs predominantly through the ductile 6063 alloy matrix phase.

Deeper exploration of the microstructural effects and phases at play in these hypereutectic Al–Si alloys provides an interesting avenue for future study. Investigating the impacts of using recycled Al alloy as an input raw material, and an associated high Fe content, could prove interesting. Previous studies have identified effective Si to have a significant impact on the performance of 6000-series aluminium alloys with high Fe content [49]. Exploration of how this effect translates to the more extreme Si levels in these hypereutectic alloys would be an interesting topic, particularly so with a view towards possible incorporation of recycled or secondary aluminium sources in the AyontEX alloys or SupremEX MMCs to increase the circularity of these high-performance materials.

5. Conclusions

A family of now commercially available high-performance hypereutectic Al–Si alloys (AyontEX™) have been developed with precise CTE matches to copper and nickel. Core material properties for the intended applications have been characterized, along with the key manufacturability considerations. The fine and homogeneous microstructure provides enhanced performance and manufacturability relative to equivalent liquid-state processed alloys. Further development work for these Al–Si alloys should be directed towards the use of mechanical alloying technology for lower CTE values, as well as testing the CTE of existing alloys over a broader temperature range. The development of additional fabricated forms via forging and extrusion for increased ductility and product form flexibility is also under investigation. Exploration of the incorporation of secondary or recycled aluminium sources as a raw material in this manufacturing process, and subsequent understanding of the effects of associated impurity elements, is an area for possible future study also.

Another potential application for Materion’s mechanical alloying technology and these alloys moving forward is additive manufacturing. Particularly for lightweight, high-precision optical mirror manufacture, the AyontEX 13 composition is interesting. More

broadly, however, the mechanical alloying process employed in this study allows for compositions to be tailored to suit the requirements for additive methods in terms of alloy and reinforcement composition and microstructures. The process also has sufficient scalability to provide an industrial solution. Due to this ability to mix a wide range of materials to produce light metal composite powders, it may be possible to produce new and novel powders as an input for additive processes. This could lead to additive manufacturing material and property options that do not exist today.

These research areas provide exciting opportunities for further exploitations of mechanical alloying technology, and powder metallurgy in general, towards developing new products to meet the needs of customers in global markets such as within the aerospace, high-performance automotive, space, and defense sectors.

Author Contributions: Conceptualization, A.T., A.F., F.G., N.F. and M.A.; Methodology, P.L., A.T. and F.G.; Project Administration, P.L. and A.F.; Investigation, P.L. and J.N.; Formal Analysis, P.L. and A.T.; Visualization, P.L.; Validation, F.G.; Writing—Original Draft Preparation, P.L.; Writing—Review & Editing, P.L., A.T., A.F., F.G., N.F. and M.A.; Supervision, A.T. and A.F. All authors have read and agreed to the published version of the manuscript.

Funding: This research received no external funding.

Data Availability Statement: The original contributions presented in the study are included in the article, further inquiries can be directed to the corresponding author.

Acknowledgments: The authors thankfully acknowledge the support provided by Outpost Technologies Inc. in the manufacture of the example mirror component presented in Figure 10b.

Conflicts of Interest: Authors P.L., A.T. and J.N. were employed by company Materion UK Limited, Author A.F. was employed by Materion Brush GmbH and Authors F.G., N.F. and M.A. were employed by Materion Corporation. We declare that the research was conducted in the absence of any commercial or financial relationships that could be construed as a potential conflict of interest.

References

1. Acreman, M.; Lewis; Farrah, N. Advanced Materials for Defense Applications-Part 2: Thermal Management. 2022. Available online: <https://www.materion.com/en/insights/blog/advanced-materials-for-defense-applications-part-2-thermal-management> (accessed on 7 May 2024).
2. Hibbard, D.L. Electroless Nickel for Optical Applications. *Adv. Mater. Opt. Precis. Struct. A Crit. Rev.* **1997**, *10289*, 173–199.
3. Rohloff, R.-R.; Gebhardt, A.; SchÄjnherr, V.; Risse, S.; Kinast, J.; Scheiding, S.; Peschel, T. A novel athermal approach for high-performance cryogenic metal optics. In Proceedings of the SPIE 7739, Modern Technologies in Space- and Ground-Based Telescopes and Instrumentation, San Diego, CA, USA, 20 July 2010.
4. Kinast, J.; Grabowski, K.; Gebhardt, A.; Rohloff, R.-R.; Risse, S.; Tünnermann, A. Dimensional Stability of Metal Optics on Nickel Plate AlSi40. In Proceedings of the SPIE 10563 International Conference on Space Optics, Tenerife, Spain, 6–10 October 2014.
5. Kinast, J.; Tünnermann, A.; Undisz, A. Dimensional Stability of Mirror Substrates Made of Silicon Particle Reinforced Aluminum. *Materials* **2022**, *15*, 2998. [[CrossRef](#)] [[PubMed](#)]
6. Zhang, R.; Zou, C.; Wei, Z.; Wang, H. Effect of High Pressure and Temperature on the Evolution of Si Phase and Eutectic Spacing in Al-20Si Alloys. *Crystals* **2021**, *11*, 705. [[CrossRef](#)]
7. Mostafa, A.; Alshabat, N. Microstructural, Mechanical and Wear Properties of Al-1.3%Si Alloy as Compared to Hypo/Hyper-Eutectic Compositions in Al-Si Alloy System. *Crystals* **2022**, *12*, 719. [[CrossRef](#)]
8. Jiandon, P.; Talangkun, S. Microstructural Modification Hardness and Surface Roughness of Hypereutectic Al-Si Alloys by a Combination of Bismuth and Phosphorus. *Crystals* **2022**, *12*, 1026. [[CrossRef](#)]
9. Rosso, M. Ceramic and Metal Matrix Composites: Route and Properties. *J. Mater. Process. Technol.* **2006**, *175*, 364–375. [[CrossRef](#)]
10. Ujah, C.O.; Kallon, D.V.V. Trends in Aluminium Matrix Composite Development. *Crystals* **2022**, *12*, 1357. [[CrossRef](#)]
11. Kruzhanov, V.; Arnhold, V. Energy Consumption in Powder Metallurgical Manufacturing. *Powder Metall.* **2012**, *55*, 14–21. [[CrossRef](#)]
12. Vine, W.J.; Goodwin, P.S. Feasibility of Synthesising Lightweight Nanophase Al Materials by Mechanical Alloying. *Mater. Sci. Forum* **2000**, 331–337, 1145–1150. [[CrossRef](#)]
13. Benjamin, J.S. Mechanical Alloying. *Sci. Am.* **1976**, *234*, 40–48. [[CrossRef](#)]
14. Suryanarayana, C.; Al-Aqeeli, N. Mechanically alloyed nanocomposites. *Prog. Mater. Sci.* **2012**, *58*, 383–502. [[CrossRef](#)]
15. Narayan, S.; Rajeshkannan, A. Workability behavior of powder metallurgy carbide reinforced aluminum composites during hot forging. *Mater. Manuf. Process.* **2015**, *30*, 1196–1201. [[CrossRef](#)]

16. Zhou, H.; Zhang, C.; Han, B.; Qiu, J.; Qin, S.; Gao, K.; Liu, J.; Sun, S.; Zhang, H. Microstructures and Mechanical Properties of Nanocrystalline AZ31 Magnesium Alloy Powders with Submicron TiB₂ Additions Prepared by Mechanical Milling. *Crystals* **2020**, *10*, 550. [[CrossRef](#)]
17. Umeda, J.; Nishimura, N.; Fujii, H.; Jia, L.; Kondoh, K. In-Situ Formed Al₃Zr Compounds Reinforced Al Composites and Tribological Application. *Crystals* **2021**, *11*, 227. [[CrossRef](#)]
18. Wu, Y.; Luo, S.; Wu, J.; Guo, B.; Wu, Z.; Chen, B.; Yu, Z.; Zhang, Z.; Li, W. Development and Characterization of CrCoNi Medium Entropy Alloy Particles Reinforced Aluminum Matrix Composite. *Crystals* **2022**, *12*, 1452. [[CrossRef](#)]
19. Arora, G.S.; Saxena, K.K.; Mohammed, K.A.; Prakash, C.; Dixit, S. Manufacturing Techniques for Mg-Based Metal Matrix Composite with Different Reinforcements. *Crystals* **2022**, *12*, 945. [[CrossRef](#)]
20. Ariff, A.M.M.; Lin, O.J.; Jung, D.-W.; Tahir, S.M.; Sulaiman, M.H. Rice Husk Ash as Pore Former and Reinforcement on the Porosity, Microstructure, and Tensile Strength of Aluminum MMC Fabricated via the Powder Metallurgy Method. *Crystals* **2022**, *12*, 1100. [[CrossRef](#)]
21. Fan, M.; Zhao, F.; Liu, Y.; Yin, S.; Peng, S.; Zhang, Z. Zinc Matrix Composites Reinforced with Partially Unzipped Carbon Nanotubes as Biodegradable Implant Materials. *Crystals* **2022**, *12*, 1110. [[CrossRef](#)]
22. Kushwaha, A.K.; Misra, M.; Menezes, P.L. Effect of Magnesium Dopant on the Grain Boundary Stability of Nanocrystalline Aluminum Powders during Cryomilling. *Crystals* **2023**, *13*, 541. [[CrossRef](#)]
23. Sübütaş, H.; Şavklıyıldız, İ. Effect of High-Energy Ball Milling in Ternary Material System of (Mg-Sn-Na). *Crystals* **2023**, *13*, 1230. [[CrossRef](#)]
24. Yan, Q.; Chen, B.; Zhou, X.; Kondoh, K.; Li, J. Effect of Metal Powder Characteristics on Structural Defects of Graphene Nanosheets in Metal Composite Powders Dispersed by Ball Milling. *Crystals* **2021**, *11*, 260. [[CrossRef](#)]
25. Nava-Dino, C.G.; Flores-De los Ríos, J.P.; Maldonado-Orozco, M.C.; Sánchez-Carrillo, M.; Bautista-Margulis, R.G.; Delgado AD, L.C.; Almeraya-Calderón, F. Electrochemical Noise Response of Cr₂Nb Powders Applying Mechanical Alloying. *Crystals* **2022**, *12*, 482. [[CrossRef](#)]
26. Gharsallah, H.I.; Azabou, M.; Khitouni, M.; Daza, J.; Suñol, J.-J. Study of the Microstructural, Thermal, and Magnetic Properties of High-Energy Ball-Milled Nanocrystalline Fe(Al). *Crystals* **2022**, *12*, 1430. [[CrossRef](#)]
27. ASM International. Milling of Brittle and Ductile Materials. In *ASM Handbook, Volume 7 Powder Metallurgy*; ASM International: Detroit, MI, USA, 2015; pp. 77–87.
28. Trautmann, M.; Ahmad, H.; Wagner, G. Influencing the Size and Shape of High-Energy Ball Milled Particle Reinforced Aluminum Alloy Powder. *Materials* **2022**, *15*, 3022. [[CrossRef](#)]
29. Raducanu, D.; Cojocaru, V.D.; Nocivin, A.; Hendea, R.E.; Ivanescu, S.; Stanciu, D.; Trisca-Rusu, C.; Serban, N.; Drob, S.I.; Campian, R.S. Microstructure Evolution during Mechanical Alloying of a Biodegradable Magnesium Alloy. *Crystals* **2022**, *12*, 1641. [[CrossRef](#)]
30. Hashiguchi, D.; Tricker, D.; Tarrant, A. Mechanically Alloyed Aluminum Metal Matrix Composites. In Proceedings of the SPIE 10372 Material Technologies and Applications to Optics Structures Components and Sub-Systems III, San Diego, CA, USA, 5 September 2017.
31. Frehn, A.; Lewis, T.; Tarrant, A. Partikelverstärkte Aluminium-Werkstoffe für Hochleistungsanwendungen. In Proceedings of the Tagungsband 40. Hagerer Symposium, Pulvermetallurgie—Vielfältige Prozesse und Werkstoffe, Hagen, Germany, 25 November 2022; pp. 309–336.
32. Hashiguchi, D.; Tricker, D.; Tarrant, A.; Campbell, J.; Pokross, C. Discontinuously reinforced aluminum MMC extrusions. *Met. Powder Rep.* **2017**, *72*, 252–258. [[CrossRef](#)]
33. Reiff-Musgrove, R.; Gaiser-Porter, M.; Gu, W.; Campbell, J.; Lewis, T.; Frehn, A.; Tarrant, A.; Tang, Y.; Burley, M.; Clyne, T.W. Indentation Plastometry of Particulate Metal Matrix Composites, Highlighting Effects of Microstructural Scale. *Adv. Eng. Mater.* **2023**, *25*, 2201479. [[CrossRef](#)]
34. Winter, L.; Hockauf, K.; Lampke, T. Temperature and Particle Size Influence on the High Cycle Fatigue Behavior of the SiC Reinforced 2124 Aluminum Alloy. *Metals* **2018**, *8*, 43. [[CrossRef](#)]
35. ASTM International. Standard Test Method for Thermal Diffusivity by the Flash Method, E1461-13. In *ASTM Volume 14.01: Quality and Statistics; Hazard Potential of Chemicals; Thermal Measurements; Manufacture of Pharmaceutical and Biopharmaceutical Products; Healthcare Informatics*; ASTM International: West Conshohocken, PA, USA, 2022.
36. Nix, F.C.; MacNair, D. The Thermal Expansion of Pure Metals: Copper, Gold, Aluminum, Nickel and Iron. *Phys. Rev.* **1941**, *60*, 597–605. [[CrossRef](#)]
37. Hidnert, P. Thermal Expansion of Copper and Some of its Important Industrial Alloys. *Sci. Pap. Bur. Stand.* **1921**, *17*, 91–159. [[CrossRef](#)]
38. Hidnert, P. Thermal Expansion of Some Nickel Alloys. *J. Res. Natl. Bur. Stand.* **1957**, *58*, 89–92. [[CrossRef](#)]
39. Bennett, S.J. The thermal expansion of copper between 300 and 700 K. *J. Phys. D Appl. Phys.* **1978**, *11*, 777–780. [[CrossRef](#)]
40. Morrell, R. *Thermal Properties of Composite Materials—Measurements, Models and Thermal Exposure Derived Changes in MMCs and CMCs*; NPL Report CMMT (A) 6; National Physical Laboratory Management Ltd.: Teddington, UK, 1995.
41. Sergo, V.; Meriani, S. Thermal Expansion and Percolation in a SiC Whisker-Reinforced Ceramic Composite. *Mater. Sci. Lett.* **1991**, *10*, 855–857. [[CrossRef](#)]

42. Few, A.; Echols, J. Aluminium metal matrix composites: A capable low-cost mirror substrate. In Proceedings of the SPIE 12677 Astronomical Optics: Design, Manufacture, and Test of Space and Ground Systems IV, San Diego, CA, USA, 4 October 2023.
43. Sweeney, M.; Colling, S.; Schmidt, J.; Few, A.; Echols, J.; Reardon, P.; Douthit, D.; Farrah, N.; Lewis, P.; Tarrant, A.; et al. Application and Testing of SupremEX®640XA and AyontEX™ 13 for Mirrors and Precision Structures, In Proceedings of the SPIE 13042 Advanced Optics for Imaging Applications: UV through LWIR IX, National Harbor, MD, USA, 23 April 2024.
44. Zhang, K.; Hemeng, Q.; Guan, H.; Zhang, J.; Zhang, X.; Xiaolin, X.; Yan, L.; Wang, C. Design and Fabrication Technology of Metal Mirrors Based on Additive Manufacturing: A Review. *Appl. Sci.* **2021**, *11*, 10630. [[CrossRef](#)]
45. Zhang, K.; Xie, X.; Wang, C.; Wang, H.; Xu, F.; Wang, H.; Zhang, X.; Guan, H.; Qu, H.; Zhang, J. Optomechanical Performances of Advanced Lightweight Mirrors Based on Additive Manufacturing. *Mircomachines* **2022**, *13*, 1334. [[CrossRef](#)] [[PubMed](#)]
46. Zhang, J.; Wang, C.; Qu, H.; Guan, H.; Wang, H.; Zhang, X.; Xie, X.; Wang, H.; Zhang, K.; Li, L. Design and Fabrication of an Additively Manufactured Aluminum Mirror with Compound Surfaces. *Materials* **2022**, *15*, 7050. [[CrossRef](#)] [[PubMed](#)]
47. Fujimori, Y.; Shimizu, M.; Kurashina, T.; Arai, S. Substrate Thermal Expansion Coefficient Effect on Cracks Induced by the High-heat Treatment of Electroplated Ni-P Films for Power Devices. *Mater. Lett.* **2023**, *350*, 134869. [[CrossRef](#)]
48. Murphy, A.; Howard, S.; Clyne, T. Characterisation of severity of particle clustering and its effect on fracture of particulate MMCs. *Mater. Sci. Technol.* **1998**, *14*, 959. [[CrossRef](#)]
49. Österreicher, J.; Arnoldt, A.; Gneiger, S.; Kunschert, G. Tolerance of Al–Mg–Si Wrought Alloys for High Fe Contents: The Role of Effective Si. *Metall. Mater. Trans. A* **2023**, *54A*, 4472–4480. [[CrossRef](#)]

Disclaimer/Publisher’s Note: The statements, opinions and data contained in all publications are solely those of the individual author(s) and contributor(s) and not of MDPI and/or the editor(s). MDPI and/or the editor(s) disclaim responsibility for any injury to people or property resulting from any ideas, methods, instructions or products referred to in the content.